Contents

List of Figures

1 Introduction

This report studies the dynamics of a mechanical system composed of two point masses connected by a linear spring, evolving in a plane in the absence of gravity. The mechanical system considered in this work is illustrated in Figure 1.

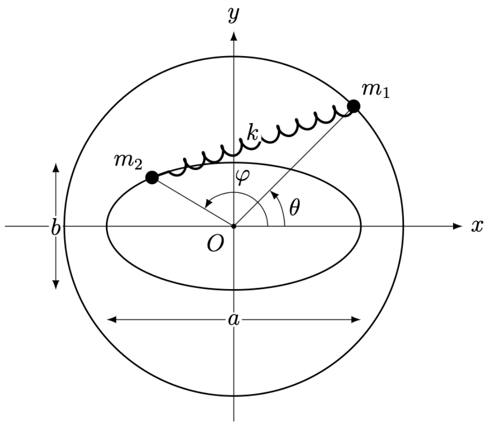

Figure 1: Schematic representation of the mechanical system.

The first mass m_1 is constrained to slide without friction along a circular trajectory of radius R centered at the origin O. The second mass m_2 is constrained to slide on an ellipse, also centered at O, whose major and minor axes are respectively a and b. Unlike m_1, the mass m_2 is subject to a viscous friction force proportional to its velocity.
The two masses are connected by a linear spring of stiffness k and natural length l_0, which introduces a coupling between the two trajectories. The system is not subject to gravity, so the only potential energy present in the system is the elastic energy stored in the spring.
The geometric constraints imposed on each mass reduce the system to two degrees of freedom, fully described by the generalized coordinates

$$q_1 = \theta, \qquad q_2 = \varphi,$$

where θ denotes the angular position of m_1 on the circle and φ denotes the parametric angle describing the position of m_2 on the ellipse.
This first report successively establishes the kinematic description of the system, derives the Lagrangian, and incorporates the friction force through the generalized force formalism.

2 Kinematic Description

The motion takes place in the plane (x, y) and the origin O is chosen as the reference point for the position vectors.

Mass m_1. Since m_1 moves on a circle of radius R, its position vector relative to the origin is given by

$$\vec{r}_1 = \begin{pmatrix} R\cos\theta \\ R\sin\theta \end{pmatrix}. \tag{1}$$

Mass m_2. The mass m_2 moves on an ellipse centered at O with semi-major axis $a/2$ and semi-minor axis $b/2$. A convenient parametric representation of the ellipse leads to the position vector

$$\vec{r}_2 = \begin{pmatrix} \frac{a}{2}\cos\varphi \\ \frac{b}{2}\sin\varphi \end{pmatrix}. \tag{2}$$

Equations (1) and (2) fully describe the spatial configuration of the two masses.

The spring connects the two masses and its deformation depends on the distance between them. The vector connecting m_1 and m_2 is defined as

$$\vec{r}_{12} = \vec{r}_1 - \vec{r}_2. \tag{3}$$

Substituting the expressions of the position vectors given in (1) and (2) into (3) yields

$$\vec{r}_{12} = \begin{pmatrix} R\cos\theta - \frac{a}{2}\cos\varphi \\ R\sin\theta - \frac{b}{2}\sin\varphi \end{pmatrix}. \tag{4}$$

The instantaneous length of the spring corresponds to the Euclidean norm of this vector as

$$l = \|\vec{r}_{12}\| = \sqrt{\left(R\cos\theta - \frac{a}{2}\cos\varphi\right)^2 + \left(R\sin\theta - \frac{b}{2}\sin\varphi\right)^2}. \tag{5}$$

The velocities of the masses are obtained by differentiating the position vectors with respect to time.

Differentiating Equation (1) gives

$$\dot{\vec{r}}_1 = \begin{pmatrix} -R\sin\theta\,\dot{\theta} \\ R\cos\theta\,\dot{\theta} \end{pmatrix}. \tag{6}$$

The squared magnitude of this velocity is therefore

$$v_1^2 = R^2\dot{\theta}^2. \tag{7}$$

Similarly, differentiating Equation (2) leads to

$$\dot{\vec{r}}_2 = \begin{pmatrix} -\frac{a}{2}\sin\varphi\,\dot{\varphi} \\ \frac{b}{2}\cos\varphi\,\dot{\varphi} \end{pmatrix}. \tag{8}$$

The squared magnitude of this velocity becomes

$$v_2^2 = \left(\frac{a^2}{4}\sin^2\varphi + \frac{b^2}{4}\cos^2\varphi\right)\dot{\varphi}^2. \tag{9}$$

3 Lagrangian Formulation

The kinetic energy of the system is the sum of the kinetic energies of the two masses,

$$K = K_1 + K_2 = \frac{1}{2}m_1R^2\dot{\theta}^2 + \frac{1}{2}m_2\left(\frac{a^2}{4}\sin^2\varphi + \frac{b^2}{4}\cos^2\varphi\right)\dot{\varphi}^2. \tag{10}$$

Since the system is not subject to gravity, the only potential energy arises from the deformation of the spring.

The elastic potential energy stored in the spring is

$$P = \frac{1}{2}k(l - l_0)^2. \tag{11}$$

The spring length l appearing in Eq. (11) is given by Eq. (5). This expression introduces a nonlinear coupling between the generalized coordinates θ and φ.

The Lagrangian of the system is defined as the difference between kinetic and potential energies,

$$L = K - P. \tag{12}$$

Substituting the expressions (10) and (11) yields the Lagrangian of the system,

$$L = \frac{1}{2}m_1R^2\dot{\theta}^2 + \frac{1}{2}m_2\left(\frac{a^2}{4}\sin^2\varphi + \frac{b^2}{4}\cos^2\varphi\right)\dot{\varphi}^2 - \frac{1}{2}k(l - l_0)^2, \tag{13}$$

where l is the instantaneous spring length defined in (5). The nonlinear coupling between θ and φ appears through l.

The equations of motion will then be obtained by applying the Euler–Lagrange equations,

$$\frac{d}{dt}\left(\frac{\partial L}{\partial \dot{q}_i}\right) - \frac{\partial L}{\partial q_i} = Q_i, \qquad i \in \{\theta, \varphi\}. \tag{14}$$

where Q_i represents the generalized forces acting on the system.

In the present system, a viscous friction force acts on the mass m_2. This friction is assumed to be proportional to the velocity of the mass and opposite to its motion. The friction force is therefore modeled as

$$\vec{F}_f = -\alpha\,\dot{\vec{r}}_2, \tag{15}$$

where α denotes the viscous damping coefficient and $\dot{\vec{r}}_2$ is the velocity of the mass m_2, given by equation (8). The generalised force associated with the coordinate φ is obtained via the virtual work principle,

$$Q_\varphi = \vec{F}_f \cdot \frac{\partial \vec{r}_2}{\partial \varphi}. \tag{16}$$

Since $\dot{\vec{r}}_2 = \dot{\varphi}\,\dfrac{\partial \vec{r}_2}{\partial \varphi}$, this reduces to

$$Q_\varphi = -\alpha\left(\frac{a^2}{4}\sin^2\varphi + \frac{b^2}{4}\cos^2\varphi\right)\dot{\varphi}. \tag{17}$$

This dissipative force introduces an additional term in the Euler–Lagrange equation associated with the coordinate φ. The equations of motion therefore become

$$\frac{d}{dt}\left(\frac{\partial L}{\partial \dot{\theta}}\right) - \frac{\partial L}{\partial \theta} = 0, \tag{18}$$

$$\frac{d}{dt}\left(\frac{\partial L}{\partial \dot{\varphi}}\right) - \frac{\partial L}{\partial \varphi} + \alpha\left(\frac{a^2}{4}\sin^2\varphi + \frac{b^2}{4}\cos^2\varphi\right)\dot{\varphi} = 0. \tag{19}$$

Since the friction acts only on the mass m_2, the coordinate θ is not directly affected by this dissipative force.

4 Equations of Motion

The equations of motion of the system are obtained by applying the Euler–Lagrange equations (14) to the Lagrangian defined in (12).

The Euler–Lagrange equation associated with the coordinate θ gives

$$m_1 R^2 \ddot{\theta} + k(l - l_0)\frac{\partial l}{\partial \theta} = 0. \tag{20}$$

Similarly, applying the Euler–Lagrange equation to the coordinate φ and including the generalised friction force (17) yields

$$\begin{aligned}&\frac{d}{dt}\left[m_2\left(\frac{a^2}{4}\sin^2\varphi + \frac{b^2}{4}\cos^2\varphi\right)\dot{\varphi}\right] - m_2\,\frac{a^2 - b^2}{4}\sin\varphi\cos\varphi\,\dot{\varphi}^2\\ &+ k(l - l_0)\frac{\partial l}{\partial \varphi} + \alpha\left(\frac{a^2}{4}\sin^2\varphi + \frac{b^2}{4}\cos^2\varphi\right)\dot{\varphi} = 0.\end{aligned} \tag{21}$$

Equations (20) and (21) form a system of two nonlinear coupled differential equations describing the dynamics of the system.

4.1 Derivatives of the spring length

To make the equations of motion explicit, the derivatives of the spring length l with respect to the generalized coordinates must be computed.
From (5), the derivative with respect to θ becomes

$$\frac{\partial l}{\partial \theta} = \frac{-R\sin\theta\left(R\cos\theta - \frac{a}{2}\cos\varphi\right) + R\cos\theta\left(R\sin\theta - \frac{b}{2}\sin\varphi\right)}{l}. \tag{22}$$

Similarly, the derivative with respect to φ is

$$\frac{\partial l}{\partial \varphi} = \frac{\frac{a}{2}\sin\varphi\left(R\cos\theta - \frac{a}{2}\cos\varphi\right) - \frac{b}{2}\cos\varphi\left(R\sin\theta - \frac{b}{2}\sin\varphi\right)}{l}. \tag{23}$$

4.2 Final Equations of Motion

Substituting the derivatives into the Euler–Lagrange equations yields the explicit equations of motion.

$$m_1 R^2 \ddot{\theta} + \frac{k(l - l_0)}{l} \Big[- R\sin\theta \left(R\cos\theta - \frac{a}{2}\cos\varphi \right) + R\cos\theta \left(R\sin\theta - \frac{b}{2}\sin\varphi \right) \Big] = 0 \tag{24}$$

$$\begin{aligned} &m_2 \left(\frac{a^2}{4}\sin^2\varphi + \frac{b^2}{4}\cos^2\varphi \right) \ddot{\varphi} + m_2 \frac{a^2 - b^2}{4} \sin\varphi\cos\varphi\, \dot{\varphi}^2 \\ &+ \frac{k(l - l_0)}{l} \Big[\frac{a}{2}\sin\varphi \left(R\cos\theta - \frac{a}{2}\cos\varphi \right) - \frac{b}{2}\cos\varphi \left(R\sin\theta - \frac{b}{2}\sin\varphi \right) \Big] + \alpha \left(\frac{a^2}{4}\sin^2\varphi + \frac{b^2}{4}\cos^2\varphi \right) \dot{\varphi} = 0 \end{aligned} \tag{25}$$

Equations (24) and (25) constitute the complete nonlinear equations of motion of the system. These equations describe the coupled dynamics of the two masses connected by the spring, including the viscous friction acting on the second mass.

5 Non-dimensionalization

Before proceeding to non-dimensionalization, the geometric parameters by the problem statement,

$$a = \frac{3}{4}R, \qquad b = \frac{1}{4}R, \qquad l_0 = R,$$

are substituted into the final equations of motion derived in the previous section. The position vectors become

$$\vec{r}_1 = \begin{pmatrix} R\cos\theta \\ R\sin\theta \end{pmatrix}, \tag{26}$$

$$\vec{r}_2 = \begin{pmatrix} \frac{3R}{8}\cos\varphi \\ \frac{R}{8}\sin\varphi \end{pmatrix}. \tag{27}$$

The instantaneous spring length is given by

$$\begin{aligned} l &= \sqrt{\left(R\cos\theta - \frac{3R}{8}\cos\varphi \right)^2 + \left(R\sin\theta - \frac{R}{8}\sin\varphi \right)^2} \\ &= R\sqrt{1 - \frac{3}{4}\cos\theta\cos\varphi - \frac{1}{4}\sin\theta\sin\varphi + \frac{1}{64}\left(9\cos^2\varphi + \sin^2\varphi\right)}. \end{aligned} \tag{28}$$

Substituting the geometric parameters into equation (24) and simplifying, the equation of motion for θ reduces to

$$\boxed{m_1 R^2 \ddot{\theta} + \frac{k\,R^2}{8}\,\frac{l - R}{l}\,(3\sin\theta\cos\varphi - \cos\theta\sin\varphi) = 0.} \tag{29}$$

Similarly, substituting the geometric parameters into equation (25) and simplifying, the equation of motion for φ reduces to

$$\boxed{\begin{aligned} &\frac{m_2\,R^2}{64}\left(9\sin^2\varphi + \cos^2\varphi\right)\ddot{\varphi} \;+\; \frac{m_2\,R^2}{8}\sin\varphi\cos\varphi\,\dot{\varphi}^2 \\ &+\; \frac{k\,R^2}{8}\,\frac{l - R}{l}\,(3\sin\varphi\cos\theta - \cos\varphi\sin\theta - \sin\varphi\cos\varphi) \\ &+\; \frac{\alpha\,R^2}{64}\left(9\sin^2\varphi + \cos^2\varphi\right)\dot{\varphi} \;=\; 0. \end{aligned}} \tag{30}$$

In order to reduce the number of independent parameters and reveal the characteristic scales governing the dynamics, the equations of motion are now written in dimensionless form. The natural length scale of the system is the radius R of the circular track, which provides the characteristic geometric length of the problem. The dimensionless time variable is introduced as

$$\tau = \omega_0\, t, \qquad \text{with} \quad \omega_0 = \sqrt{\frac{k}{m_1}}. \tag{31}$$

The quantity ω_0 corresponds to the natural frequency of a mass–spring oscillator with mass m_1 and stiffness k, which sets the characteristic time scale of the system. With this choice, the time derivatives transform according to

$$\dot{(\cdot)} = \omega_0\,(\cdot)', \qquad \ddot{(\cdot)} = \omega_0^2\,(\cdot)'',$$

where the prime notation $(\cdot)'$ denotes differentiation with respect to the dimensionless time τ.

Two dimensionless parameters naturally emerge from this process. The first is the mass ratio

$$\mu = \frac{m_2}{m_1}\,, \tag{32}$$

which characterizes the relative inertia of the two particles. When $\mu \ll 1$, the second mass responds almost instantaneously to the spring force and the dynamics are dominated by the motion of m_1. Conversely, when $\mu \gg 1$, the elliptical mass is much heavier and the circular mass acts as a light oscillator driven by the motion of m_2.

The second parameter is the dimensionless friction coefficient

$$\beta = \frac{\alpha}{m_1\,\omega_0} = \frac{\alpha}{\sqrt{k\,m_1}}\,, \tag{33}$$

which measures the strength of the viscous dissipation acting on m_2 relative to the elastic restoring force. The limit $\beta = 0$ corresponds to the frictionless system, while large values of β indicate that the motion of m_2 is strongly damped.

With this choice of reference quantities, the common factor $m_1 R^2 \omega_0^2 = kR^2$ can be factored out of every term in equations (29) and (30), leaving the system expressed solely in terms of μ, β and the dimensionless time τ.

The dimensionless equation of motion for θ reads

$$\boxed{\theta'' + \frac{1}{8}\,\frac{l-R}{l}\,(3\sin\theta\cos\varphi - \cos\theta\sin\varphi) = 0.} \tag{34}$$

Proceeding similarly with equation (30), the dimensionless equation of motion for φ reads

$$\boxed{\begin{aligned} &\frac{\mu}{64}\left(9\sin^2\varphi + \cos^2\varphi\right)\varphi'' \;+\; \frac{\mu}{8}\sin\varphi\cos\varphi\,(\varphi')^2 \\ &+\; \frac{1}{8}\,\frac{l-R}{l}\,(3\sin\varphi\cos\theta - \cos\varphi\sin\theta - \sin\varphi\cos\varphi) \\ &+\; \frac{\beta}{64}\left(9\sin^2\varphi + \cos^2\varphi\right)\varphi' \;=\; 0. \end{aligned}} \tag{35}$$

In both equations, the ratio $(l-R)/l$ involves the dimensionless spring length l/R, which is directly obtained from equation (28) as

$$\frac{l}{R} = \sqrt{1 - \frac{3}{4}\cos\theta\cos\varphi - \frac{1}{4}\sin\theta\sin\varphi + \frac{1}{64}\left(9\cos^2\varphi + \sin^2\varphi\right)}\,, \tag{36}$$

so that the dimensionless spring extension can be evaluated as

$$\frac{l-R}{l} = 1 - \frac{1}{l/R}\,. \tag{37}$$

The non-dimensionalization reveals that the dynamics of the system are entirely governed by only two parameters: the mass ratio μ and the damping coefficient β.
Finally, the dimensionless total energy of the system is obtained from equations (10) and (11) following the same procedure. This gives

$$\hat{E} = \frac{1}{2}(\theta')^2 + \frac{\mu}{128}\left(9\sin^2\varphi + \cos^2\varphi\right)(\varphi')^2 + \frac{1}{2}\left(\frac{l}{R} - 1\right)^2. \tag{38}$$

Each term is non-negative, so that $\hat{E} \geq 0$ at all times. In the absence of friction ($\beta = 0$), the total energy $\hat{E}$ is conserved.

When friction is present ($\beta > 0$), the rate of change of the total energy can be derived by multiplying the dimensionless equation of motion for θ (34) by θ' and the dimensionless equation of motion for φ (35) by φ'. Starting with the equation for θ,

$$\theta'\,\theta'' + \frac{1}{8}\,\frac{l-R}{l}\,(3\sin\theta\cos\varphi - \cos\theta\sin\varphi)\,\theta' = 0. \tag{39}$$

The first term can be recognized as

$$\theta'\,\theta'' = \frac{d}{d\tau}\left(\frac{1}{2}(\theta')^2\right), \tag{40}$$

which is the time derivative of the dimensionless kinetic energy of m_1. Similarly, multiplying the equation for φ by φ' gives

$$\begin{aligned} &\frac{\mu}{64}\left(9\sin^2\varphi + \cos^2\varphi\right)\varphi'\,\varphi'' \;+\; \frac{\mu}{8}\sin\varphi\cos\varphi\,(\varphi')^3 \\ &+\; \frac{1}{8}\,\frac{l-R}{l}\,(3\sin\varphi\cos\theta - \cos\varphi\sin\theta - \sin\varphi\cos\varphi)\,\varphi' \\ &+\; \frac{\beta}{64}\left(9\sin^2\varphi + \cos^2\varphi\right)(\varphi')^2 \;=\; 0. \end{aligned} \tag{41}$$

The first two terms correspond to the time derivative of the dimensionless kinetic energy of m_2,

$$\frac{d}{d\tau}\left[\frac{\mu}{128}\left(9\sin^2\varphi + \cos^2\varphi\right)(\varphi')^2\right] = \frac{\mu}{64}\left(9\sin^2\varphi + \cos^2\varphi\right)\varphi'\,\varphi'' + \frac{\mu}{8}\sin\varphi\cos\varphi\,(\varphi')^3, \tag{42}$$

where the second contribution arises from differentiating the φ-dependent geometric factor. Furthermore, the spring-related terms in equations (39) and (41) combine to give the time derivative of the dimensionless potential energy,

$$\frac{d}{d\tau}\left[\frac{1}{2}\left(\frac{l}{R} - 1\right)^2\right] = \frac{l-R}{l}\left[\frac{1}{8}\,(3\sin\theta\cos\varphi - \cos\theta\sin\varphi)\,\theta' + \frac{1}{8}\,(3\sin\varphi\cos\theta - \cos\varphi\sin\theta - \sin\varphi\cos\varphi)\,\varphi'\right]. \tag{43}$$

Adding equations (39) and (41) and using the identities (40), (42) and (43), all conservative terms regroup into $d\hat{E}/d\tau$ and only the friction term remains. This yields

$$\boxed{\frac{d\hat{E}}{d\tau} = -\frac{\beta}{64}\left(9\sin^2\varphi + \cos^2\varphi\right)(\varphi')^2 \;\le\; 0\,,} \tag{44}$$

which confirms that the viscous force acting on m_2 is the only source of dissipation in the system. The inequality follows from the fact that the geometric factor $\left(9\sin^2\varphi + \cos^2\varphi\right)$ is strictly positive for all values of φ.

6 Numerical Resolution and Analysis

The dimensionless equations of motion (34) and (35) do not admit closed-form solutions: the trigonometric coupling terms ($\sin\theta\cos\varphi$, $\cos\theta\sin\varphi$), the geometric factor $g(\varphi)$ appearing at the denominator of the φ acceleration, and the nonlinear dependence of the spring ratio $(l-R)/l$ on both angles together rule out integration in elementary functions. This section therefore integrates the equations numerically, validates the implementation, and investigates the system dynamics. All simulations use $\mu = 1$ (equal masses) unless stated otherwise.

6.1 State-space formulation and integration method

The system is recast as a first-order system $\mathbf{y}' = \mathbf{f}(\mathbf{y})$ by introducing the state vector

$$\mathbf{y} = \begin{pmatrix} \theta \\ \varphi \\ \theta' \\ \varphi' \end{pmatrix}, \tag{45}$$

where the prime denotes differentiation with respect to τ. The right-hand side of this system is

$$\mathbf{f}(\mathbf{y}) = \begin{pmatrix} \theta' \\ \varphi' \\ F_\theta(\theta,\varphi) \\ F_\varphi(\theta,\varphi,\varphi') \end{pmatrix}, \tag{46}$$

where the first two components are the velocities already present in $\mathbf{y}$, and the last two are the accelerations F_θ and F_φ, obtained by isolating θ'' and φ'' from the dimensionless equations of motion (34) and (35). Defining the geometric factor $g(\varphi) = 9\sin^2\varphi + \cos^2\varphi > 0$, these read

$$F_\theta = -\frac{1}{8}\frac{l-R}{l}\left(3\sin\theta\cos\varphi - \cos\theta\sin\varphi\right), \tag{47}$$

$$F_\varphi = -\frac{64}{\mu\, g(\varphi)}\left[\frac{\mu}{8}\sin\varphi\cos\varphi\,(\varphi')^2 + \frac{1}{8}\frac{l-R}{l}(3\sin\varphi\cos\theta - \cos\varphi\sin\theta - \sin\varphi\cos\varphi) + \frac{\beta}{64}\,g(\varphi)\,\varphi'\right]. \tag{48}$$

The system is integrated with the adaptive RK45 method from `scipy.integrate.solve_ivp` Virtanen et al. (2020), with `rtol` $= 10^{-10}$ and `atol` $= 10^{-12}$. An interactive web-based simulator[1] was developed in parallel and used to explore the parameter space and select the initial conditions.

6.2 Initial conditions

All simulations use the same initial conditions:

$$\theta_0 = \frac{\pi}{2}\ \text{rad}, \quad \varphi_0 = 0\ \text{rad}, \quad \theta'_0 = 0.5\ \text{rad}/\tau, \quad \varphi'_0 = 4.0\ \text{rad}/\tau, \tag{49}$$

where positive angular velocities correspond to counter-clockwise motion in the (x, y) plane. The initial energy is $\hat{E}_0 \approx 0.252$, split equally between $K_1 \approx 50\%$ and $K_2 \approx 50\%$, with a small contribution from the spring ($P \approx 1\%$). This balanced partition ensures that neither mass dominates the dynamics and that both the direct dissipation channel (through K_2) and the indirect channel (through the spring coupling, $K_1 \to P \to K_2$) are active from the start.

6.3 Validation: energy conservation

Figure 2 monitors the total energy and its relative drift for $\beta = 0$.

Observation. The energy remains constant at $\hat{E}_0 = 0.2523$ over the entire simulation. The relative drift $(\hat{E} - \hat{E}_0)/\hat{E}_0$ stays below 5×10^{-8}.

Conclusion. Since the analytical derivation in Section 5 guarantees $\mathrm{d}\hat{E}/\mathrm{d}\tau = 0$ when $\beta = 0$, the near-perfect conservation of $\hat{E}$ in the numerical solution confirms that the equations of motion have been correctly implemented and that the state-space formulation (46)–(48) is consistent with the Lagrangian model.

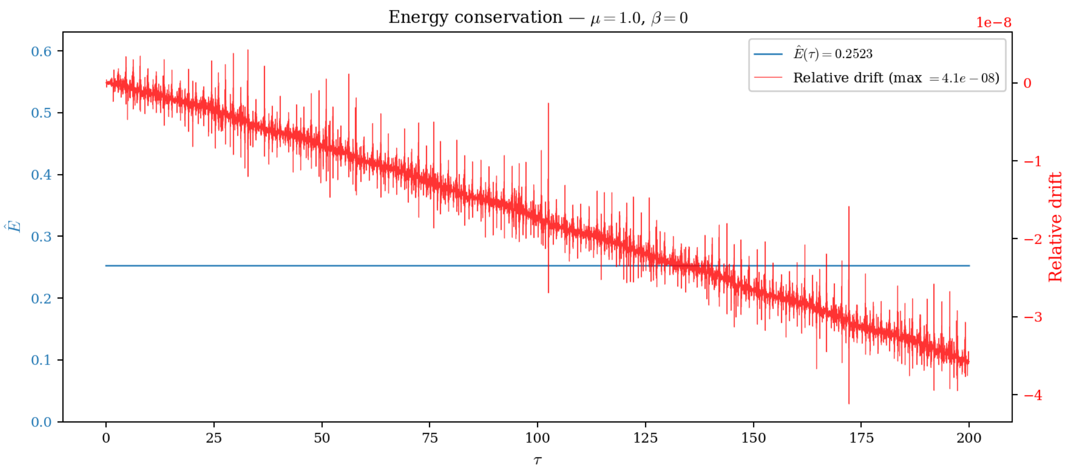

Figure 2: Energy conservation ($\mu = 1$, $\beta = 0$). Blue: total energy (constant). Red: relative drift ($< 5 \times 10^{-8}$).

6.4 System response and energy exchanges

Figure 3 compares the conservative ($\beta = 0$) and dissipative ($\beta = 0.5$) responses.

Observation — conservative case (left). Both angles grow monotonically: the masses rotate continuously on their constraint curves. Over $\tau = 200$, m_1 completes approximately 16 full turns ($\theta \approx 100$ rad) while m_2

[1] https://valentinangenot.github.io/simulation_modelling/

completes about 56 turns ($\varphi \approx 350$ rad). The faster rotation of m_2 reflects both the higher initial velocity ($\varphi'_0 = 4$ vs. $\theta'_0 = 0.5$) and the smaller size of the ellipse, which requires less displacement per radian. Despite the continuous rotation, the total energy $\hat{E}$ remains constant, while K_1, K_2 and P oscillate: each time the angular separation between the two masses changes, the spring stretches or compresses, periodically converting kinetic energy into potential energy and vice versa.

Observation — dissipative case (right). With $\beta = 0.5$, both angles initially grow but their behaviour differs markedly from the conservative case. The mass m_2 does not rotate continuously: φ oscillates back and forth with decreasing amplitude, reversing direction several times before converging to a final position ($\varphi \to 6$ rad). The mass m_1 undergoes a few turns ($\theta \to 22$ rad) before also coming to rest. The total energy decays to zero within approximately $\tau \approx 100$. The energy panel reveals that K_2 is dissipated first, since the friction acts directly on m_2. The kinetic energy K_1 of the frictionless mass persists longer, decaying only as the spring coupling progressively transfers it to m_2. The potential energy P vanishes last, once both masses have stopped and the spring has relaxed.

Conclusion. In the conservative case, the spring does not prevent the masses from ro tating, but periodically modulates their velocities, producing the oscillations visible in the energy decomposition. In the dissipative case, friction on m_2 first arrests its rotation, then the spring coupling gradually extracts the remaining kinetic energy from m_1 until both masses come to rest. The indirect dissipation pathway $K_1 \to P \to K_2 \to$ friction is visible in the energy panel: K_1 persists longer than K_2 because it can only be dissipated through the spring coupling.

Equilibrium configuration. At rest, all conservative terms in equation (44) vanish and the spring must be relaxed, so that $l = l_0 = R$, i.e. $\lambda = 1$. Substituting this condition in equation (36) and squaring yields the analytical equilibrium relation between θ and φ,

$$\tfrac{3}{4}\cos\theta_{\text{eq}}\cos\varphi_{\text{eq}} + \tfrac{1}{4}\sin\theta_{\text{eq}}\sin\varphi_{\text{eq}} = \frac{9\cos^2\varphi_{\text{eq}} + \sin^2\varphi_{\text{eq}}}{64}\,. \tag{50}$$

Evaluating this expression at the final state of the simulation ($\theta \to 23.574$ rad, $\varphi \to 5.834$ rad, obtained by extending the integration to $\tau = 500$ until $|\theta'|, |\varphi'| < 10^{-13}$) gives $\lambda = 1$ to machine precision and a residual of equation (50) below 10^{-15}, confirming that the numerical solution converges to a configuration where the spring is exactly relaxed.

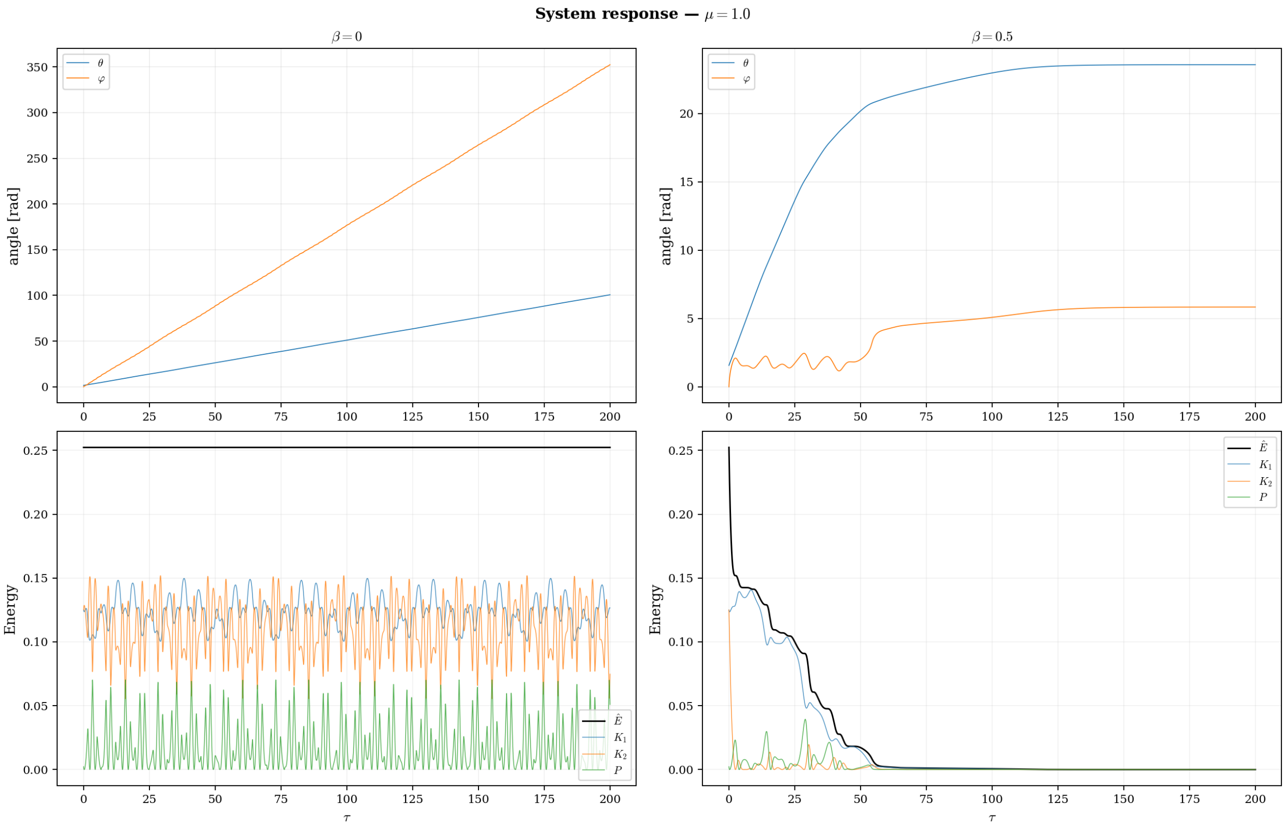

Figure 3: System response ($\mu = 1$). Left: $\beta = 0$. Right: $\beta = 0.5$. Top: angular positions. Bottom: energy decomposition.

6.5 Influence of the damping coefficient β

Figure 4 shows the total energy evolution for six values of β ranging from 0 to 20.

Observation. For $\beta = 0$, the energy is constant. For $\beta = 0.1$ and 0.5, the energy decays efficiently toward zero. For $\beta = 2$, the decay is slower. For $\beta = 8$ and 20, a significant fraction of the initial energy persists at $\tau = 200$.

Interpretation. This counter-intuitive result, where more friction leads to *less* dissipation, arises because the friction acts only on m_2 and the dissipation power $\frac{\beta}{64}\, g(\varphi)\, (\varphi')^2$ is *quadratic* in φ'. For the 50% of energy initially stored in K_1 to be dissipated, it must first be transferred to m_2 through the spring coupling. When β is moderate, m_2 is free to oscillate in response to the spring force, and each oscillation cycle dissipates a fraction of the energy received. When β is large, the friction force on m_2 dominates the spring force and the equation of motion for φ reduces, at leading order, to a balance between the spring driving and the linear friction term $\frac{\beta}{64}\, g(\varphi)\, \varphi'$: the mass m_2 reaches a low *quasi-static* velocity $\varphi' = \mathcal{O}(1/\beta)$, which gives an instantaneous dissipation power in $\mathcal{O}(\beta \cdot 1/\beta^2) = \mathcal{O}(1/\beta)$. The combined effect is that the faster the friction stiffens the response, the smaller the velocity becomes, and the quadratic dependence makes the product vanish. The kinetic energy of m_1 therefore remains trapped.

Conclusion. There exists an optimal range of β that allows efficient dissipation of the total energy. This is a structural property of systems where damping is localised on a subset of the degrees of freedom.

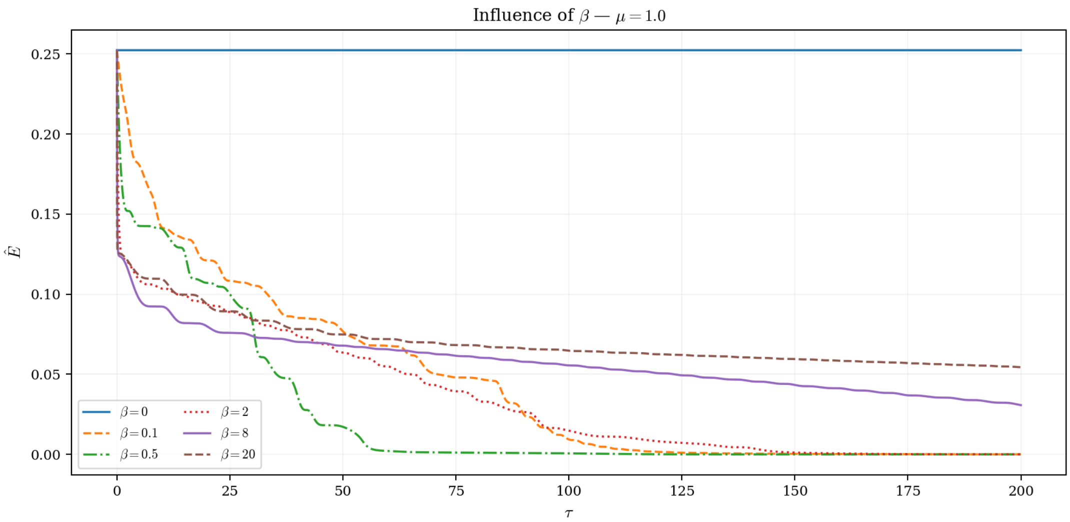

Figure 4: Influence of β on total energy ($\mu = 1$). Moderate β dissipates efficiently; large β traps energy by immobilizing m_2.

6.6 Influence of the mass ratio μ

Figure 5 shows the energy evolution for four values of μ at $\beta = 0.5$.

Observation. For $\mu = 0.1$, 0.5, 1 and 2, the energy decays to zero within approximately $\tau \approx 50$. All three curves exhibit the same qualitative behaviour; only the initial energy level differs. Starting at $\mu = 5$, the dissipation becomes visibly slower and does not reach zero within the simulation window.

Interpretation. The mass ratio μ affects the dissipation through two competing mechanisms. First, the initial energy increases with μ because $K_2 = \frac{\mu}{128}\, g(\varphi_0)\, (\varphi_0')^2$ is proportional to μ, so there is more energy to dissipate. Second, the effective inertia of m_2 on the ellipse scales as $\frac{\mu}{64}\, g(\varphi)$, which is the coefficient of φ'' in equation (35). A larger μ increases this inertia, reducing the angular acceleration that the spring force can impart to m_2. The result is a lower φ' for a given spring force, and therefore a lower instantaneous dissipation power $\frac{\beta}{64}\, g(\varphi)\, (\varphi')^2$. Conversely, a light m_2 ($\mu \ll 1$) accelerates easily, reaches high angular velocities, and dissipates energy rapidly. For $\mu = 2$, 5 and 10, the analytical result (44) ensures that the total energy cannot increase for any $\beta > 0$. However, the simulations show that the approach to rest can occur on a much longer time scale than the main simulation window $\tau \leq 200$. Extended integrations confirm this slow asymptotic decay: for $\mu = 2$ and $\mu = 5$ at $\tau = 2000$, and for $\mu = 10$ at $\tau = 5000$, the total energy reaches $\hat{E}/\hat{E}_0 < 10^{-25}$.

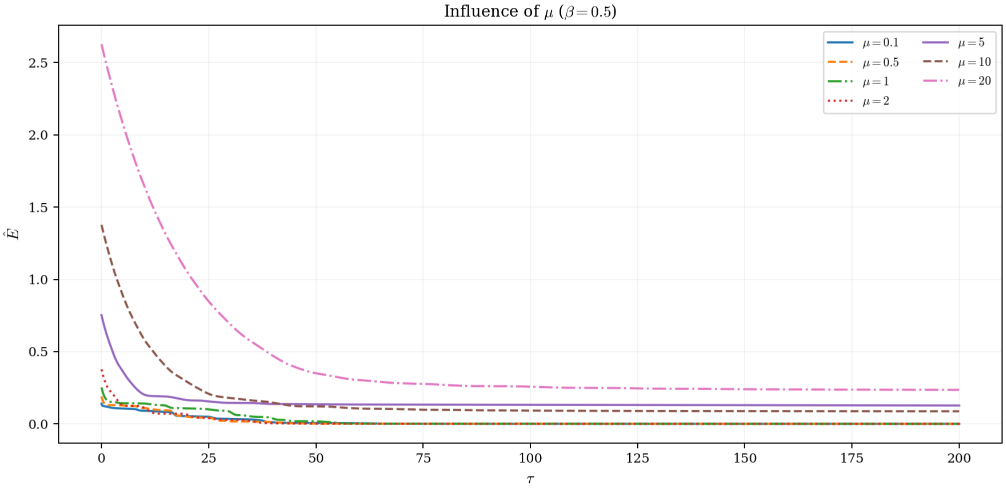

Figure 5: Influence of μ on total energy ($\beta = 0.5$). Lighter m_2 dissipates energy faster.

6.7 Phase portraits

Figure 6 compares the phase-space trajectories for $\beta = 0$, $\beta = 0.5$ and $\beta = 5$.

Observation — conservative case (left). Since the masses rotate continuously, the phase portraits are not closed orbits but horizontal bands swept from left to right. For m_1 (top left), the angular velocity θ' oscillates within a narrow band (≈ 0.45–0.55) around its initial value $\theta'_0 = 0.5$. For m_2 (bottom left), the band is much wider ($\varphi' \approx 1.2$–4.2). The dominant cause of this width is purely geometric: in the absence of coupling, $K_2 = \frac{\mu}{128}\, g(\varphi)\, (\varphi')^2$ defined in (38) would be exactly conserved, giving $\varphi' = \varphi'_0/\sqrt{g(\varphi)}$ which sweeps from $\varphi'_0 = 4$ at $\varphi = 0, \pi$ (where $g = 1$) down to $\varphi'_0/3 \approx 1.33$ at $\varphi = \pm\pi/2$ (where $g = 9$). The factor of nine variation of g along the ellipse therefore alone accounts for most of the observed band, while the spring coupling adds a small additional widening (from [1.33, 4] to [1.2, 4.2]) by exchanging a fraction of K_2 with K_1 and the spring. The narrow band of θ' reflects the converse situation: $K_1 = \frac{1}{2}(\theta')^2$ has no θ-dependent geometric factor, so the variations of θ' are driven solely by energy exchange with the spring and m_2. Since the bulk of the AC fluctuations are absorbed by the geometrically modulated K_2, only a small fraction is reflected in θ', hence the tight band $\Delta\theta' \approx \pm 0.05$ around θ'_0.

Observation — moderate damping ($\beta = 0.5$, centre). Friction decelerates m_2 first: it reverses direction several times, oscillating back and forth on the ellipse until it stops. The mass m_1, with no friction, decelerates more slowly through the spring coupling and covers progressively shorter arcs before also coming to rest.

Observation — strong damping ($\beta = 5$, right). The phase portrait of m_2 exhibits a characteristic L-shape: φ' drops sharply from 4 to nearly 0 while φ increases only modestly to about 0.6 rad, after which the trajectory creeps slowly along the $\varphi' \approx 0$ axis until m_2 reaches its rest position near $\varphi_{\mathrm{eq}} \approx 1.6$ rad. The angular *velocity* of m_2 collapses almost immediately, but its angular *position* still drifts by roughly $\pi/2$ before equilibrium is reached. This is the quasi-static regime discussed in Section 6.5: m_2 is so heavily damped that the friction force balances the spring force at very low speed, making the instantaneous dissipation power $\frac{\beta}{64}\, g(\varphi)\, (\varphi')^2$ from (44) small. For m_1, θ' decreases monotonically from 0.5 to ≈ 0.07 while θ reaches ≈ 60 rad: energy is still being drained through the indirect channel $K_1 \to P \to K_2 \to$ friction, but much more slowly than at $\beta = 0.5$. A large β does not prevent dissipation, it simply stretches its time scale well beyond the simulation window.

Conclusion. The phase portraits reveal the asymmetry of the dissipation mechanism. The mass m_2, subject to friction, loses most of its velocity quickly (the steep initial drop in φ'). The mass m_1, with no friction, decelerates gradually as the spring coupling slowly drains its kinetic energy. The small loops visible for m_2 near the origin correspond to the back-and-forth oscillations observed in the time-domain response (Figure 3). The comparison between the three columns makes visible the non-monotonic effect of β already identified in Section 6.5.

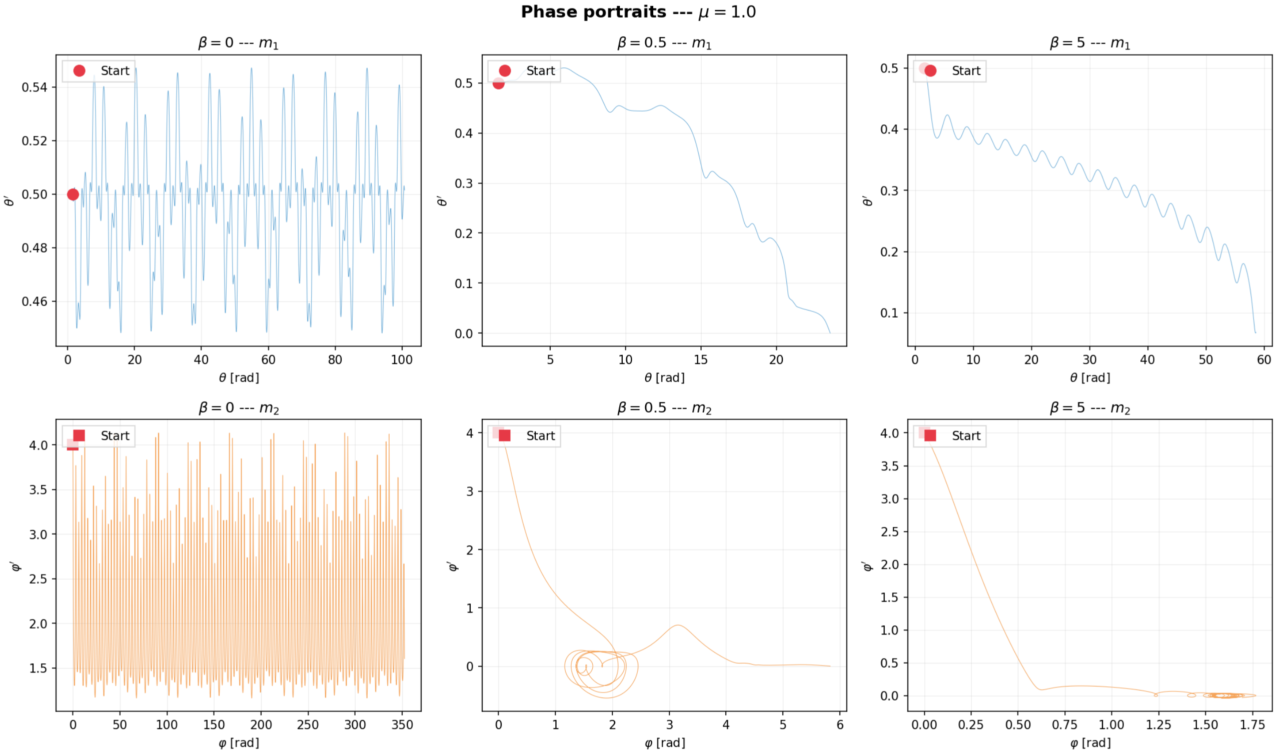

Figure 6: Phase portraits ($\mu = 1$). Left: $\beta = 0$ (dense quasi-periodic orbits). Centre: $\beta = 0.5$ (inward spirals). Right: $\beta = 5$ (L-shaped trajectory of m_2: rapid velocity collapse followed by slow drift to equilibrium; m_1 keeps rotating). Top: m_1. Bottom: m_2.

Folded representation. In the conservative case, the unfolded portraits above collapse into dense horizontal bands because θ and φ grow unboundedly. Since the dynamics are 2π-periodic in both angles, a more informative view is obtained by folding them to the fundamental interval $[-\pi, \pi]$, using $\theta \mapsto \theta \bmod 2\pi$ and $\varphi \mapsto \varphi \bmod 2\pi$ (with 2π jumps removed by inserting breaks in the line). Figure 7 shows the resulting portraits.

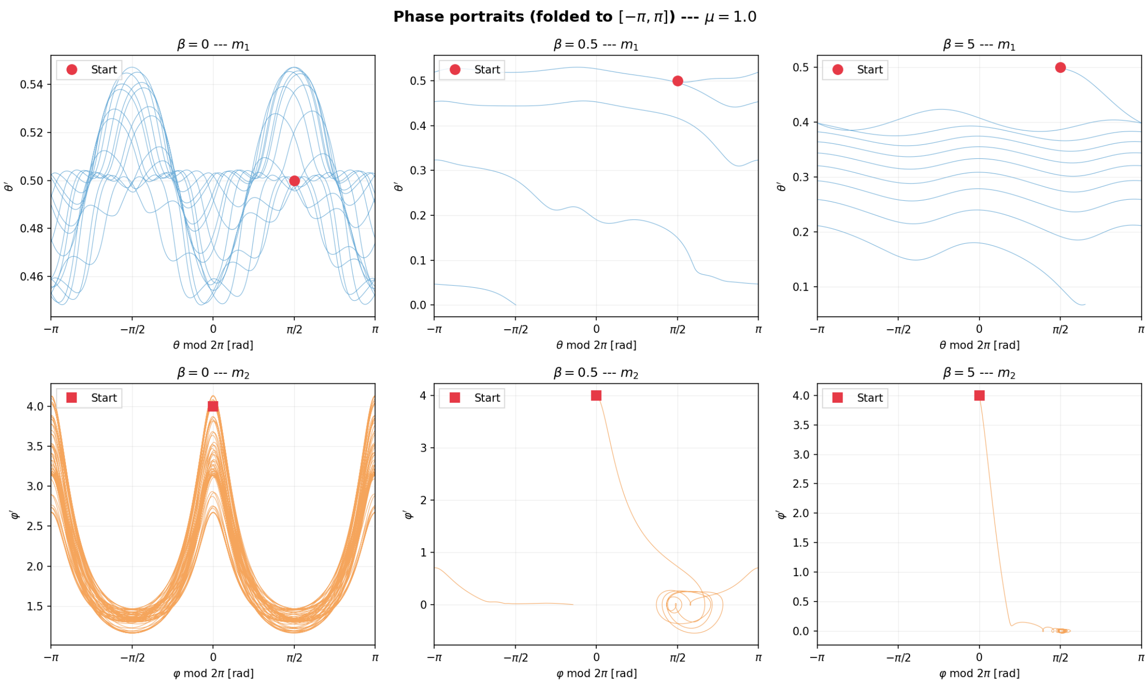

Figure 7: Phase portraits folded to $[-\pi, \pi]$ ($\mu = 1$). Left: $\beta = 0$. Centre: $\beta = 0.5$. Right: $\beta = 5$. Top: m_1. Bottom: m_2.

Observation — conservative case (left). The quasi-periodic structure of the orbits, hidden in Figure 6, becomes clearly visible after folding. For m_1, the folded portrait displays a family of modulated curves that resembles a distorted pendulum phase plane, reflecting the beating between the two natural frequencies of the coupled system. The modulation is symmetric around $\theta \bmod 2\pi = \pi/2$, the initial angular position of m_1. For m_2, the portrait is concentrated around $\varphi \bmod 2\pi = 0$, where φ' reaches its maxima (≈ 4.1): this is the configuration in which m_2 is closest to m_1 on the ellipse and the spring force accelerates it most strongly. The symmetric valleys at $\varphi \bmod 2\pi = \pm\pi$ correspond to the opposite side of the ellipse, where the spring is less stretched and m_2 slows down.

Observation — moderate damping (centre). The inward spiral of Figure 6 is replaced by a more compact trajectory. For m_2, the folded view makes the small oscillations near the rest state clearly visible: the mass circles around $\varphi_{\text{eq}} \bmod 2\pi \approx -0.45$ rad before converging to it, matching the equilibrium relation (50) derived in Section 6.4. For m_1, the orbit descends gradually from $\theta' = 0.5$ to $\theta' = 0$ while sweeping multiple times over $[-\pi, \pi]$, confirming that m_1 keeps rotating on the circle long after m_2 has essentially settled.

Observation — strong damping (right). The m_2 portrait shows the L-shape of Figure 6: a steep drop of φ' from 4 to nearly 0, followed by a horizontal segment along which φ drifts toward its equilibrium value $\varphi_{\text{eq}} \bmod 2\pi \approx 1.6$ rad. The folded view confirms that m_2 does *not* stay near its initial position: only its velocity collapses, while its position migrates by roughly $\pi/2$ along the ellipse before the system locks. In contrast, the m_1 portrait shows the same kind of dense horizontal bands as the conservative case (left), but at progressively lower θ' values, directly visualising the energy trapped in m_1 that fails to be dissipated.

Conclusion. Folding the angles modulo 2π makes the geometric structure of the dynamics directly readable. The conservative case reveals its underlying torus structure, the moderate dissipation case exhibits a clean convergence toward the equilibrium position, and the strong damping case shows how the energy is split between a slowly-creeping m_2 and a still-rotating m_1.

7 Frequency analysis

This section characterises the conservative dynamics ($\beta = 0$) in the frequency domain. In the absence of gravity, the angles θ and φ grow unboundedly and are not good candidates for a Fourier analysis. The angular velocities $\theta'(\tau)$ and $\varphi'(\tau)$, on the other hand, remain bounded and oscillate around their mean value (Figures 6 and 7); they are the natural signals to analyse.

Methodology

For each simulation, the signal $s(\tau)$ (either θ' or φ') is sampled on a uniform grid of $N = 2^{15}$ points over $\tau \in [0, T)$, giving a spacing $\Delta\tau = T/N$ with $T = 400$. The mean is subtracted to remove the DC component, and a Hann window

$$w(\tau) = \tfrac{1}{2}\left(1 - \cos\frac{2\pi\,(\tau - \tau_{\min})}{T}\right) \tag{51}$$

is applied to attenuate spectral leakage due to the finite observation window. The windowed signal is transformed via a real FFT (`numpy.fft.rfft`), yielding the half-spectrum

$$G_k = \sum_{n=0}^{N-1} s[n]\,w[n]\,e^{-\mathrm{i}\,2\pi k n/N}, \qquad \nu_k = \frac{k}{N\,\Delta\tau} = \frac{k}{T}. \tag{52}$$

The frequency resolution is $\Delta\nu = 1/T = 2.5 \times 10^{-3}$ cycles per unit τ and the Nyquist frequency is $\nu_{\max} = 1/(2\,\Delta\tau) \approx 41$, well above the frequencies of interest. Each spectrum is normalised by its own maximum to focus on shape rather than absolute amplitude.

Reference case

Figure 8 shows the spectra of θ' and φ' for the reference parameters of the rest of the report ($\mu = 1$, $\theta_0 = \pi/2$, $\varphi_0 = 0$, $\theta'_0 = 0.5$, $\varphi'_0 = 4$).

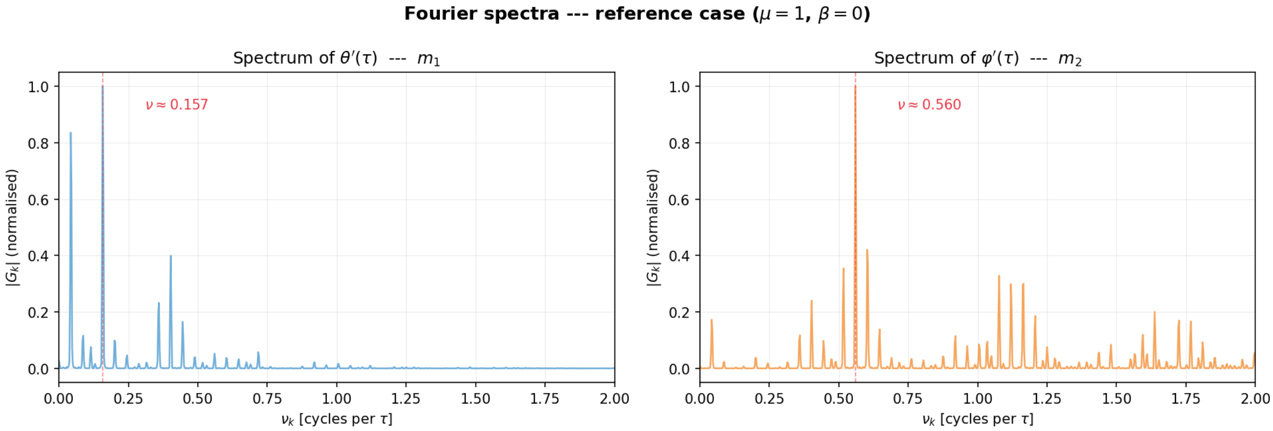

Figure 8: Fourier spectra of $\theta'(\tau)$ (blue) and $\varphi'(\tau)$ (orange) for the reference case ($\mu = 1$, $\beta = 0$). Each spectrum is normalised by its own maximum. The dashed red line marks the dominant frequency.

The dominant frequency of θ' is $\nu_\theta \approx 0.157$ cycles per unit τ, and that of φ' is $\nu_\varphi \approx 0.560$. Both spectra also contain a comb of secondary peaks that are not harmonics of a single frequency but appear at sums and differences of ν_θ and ν_φ. This is the typical signature of quasi-periodic motion on a two-frequency torus; a formal identification of such an invariant torus, through Poincaré sections or frequency maps, is not pursued here.

Origin of the dominant peaks. The two dominant frequencies are not the rotation frequencies of the masses, but approximately *twice* their time-averaged rotation frequencies. Measuring the time-averages from the simulation gives $\langle\theta'\rangle \approx 0.496$ and $\langle\varphi'\rangle \approx 1.762$, so that

$$\frac{2\langle\theta'\rangle}{2\pi} = \frac{\langle\theta'\rangle}{\pi} \approx 0.158, \qquad \frac{2\langle\varphi'\rangle}{2\pi} = \frac{\langle\varphi'\rangle}{\pi} \approx 0.561, \tag{53}$$

in close agreement with the observed peaks. The relation $\nu \approx \langle\dot{q}\rangle/\pi$ is referred to in the rest of this section as an empirical relation: it is reported here as an observation valid in the regimes covered below, not as a general theorem.

The factor of two has a clear physical interpretation, different for each velocity. For φ', it is geometric. The factor $g(\varphi)$ that appears throughout the dimensionless equations of motion (35) and the energy (38) can be rewritten as

$$g(\varphi) = 9\sin^2\varphi + \cos^2\varphi = 5 - 4\cos(2\varphi), \tag{54}$$

which is π-periodic in φ. As φ rotates over a full 2π, g therefore goes through two cycles, and any quantity proportional to g (in particular φ' itself, through the approximate conservation $g(\varphi)\,(\varphi')^2 \approx \text{const}$) is modulated at twice the rotation frequency. This matches the observed peak position. For θ', the factor of two follows from the nonlinear structure of the spring force. The bracket $3\sin\theta\cos\varphi - \cos\theta\sin\varphi$ that drives the equation of motion for θ in (34) decomposes as

$$3\sin\theta\cos\varphi - \cos\theta\sin\varphi = \sin(\theta+\varphi) + 2\sin(\theta-\varphi), \tag{55}$$

so that the elementary forcing terms have frequencies $\langle\theta'\rangle \pm \langle\varphi'\rangle$. When (55) is multiplied by the factor $(l-R)/l$ defined in (37), which itself contains $\cos(\theta\pm\varphi)$ contributions, the resulting nonlinear product produces components at frequency 2θ, matching the observed peak at $\langle\theta'\rangle/\pi$. The precise amplitude of this peak would require an expansion of $(l-R)/l$ to higher order, which is not pursued here.

The ratio ν_φ/ν_θ. Combining the two relations of (53) gives

$$\frac{\nu_\varphi}{\nu_\theta} = \frac{\langle\varphi'\rangle}{\langle\theta'\rangle} \approx 3.55, \tag{56}$$

which is the ratio of the time-averaged angular velocities, *not* the ratio of initial velocities $\varphi'_0/\theta'_0 = 8$. The substantial gap between $\langle\varphi'\rangle \approx 1.76$ and $\varphi'_0 = 4$ is a direct consequence of the geometric slowdown imposed by $g(\varphi)$: m_2 spends most of the period near the long axis of the ellipse, where $g = 9$ and φ' is reduced by a factor of three, so that the time-average is strongly biased toward these slow regions.

Influence of the mass ratio μ

Figure 9 compares the spectra for $\mu \in \{0.1, 1, 10\}$ with the reference initial conditions.

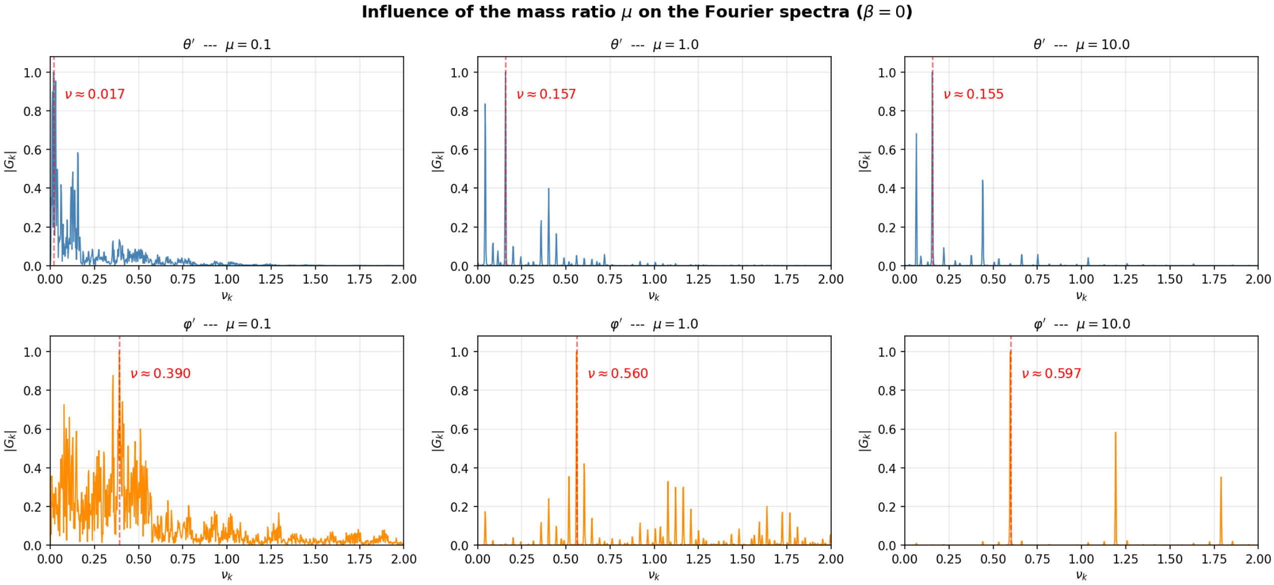

Figure 9: Influence of the mass ratio μ on the Fourier spectra of θ' (top) and φ' (bottom) with the reference initial conditions and $\beta = 0$.

The evolution with μ has two facets. When μ is small ($\mu = 0.1$, m_2 light), the effective inertia of m_2 on the ellipse, $\frac{\mu}{64}\, g(\varphi)$, becomes very small and the spring coupling accelerates m_2 strongly. The resulting dynamics is highly irregular and the spectrum of both velocities is a broad continuum without a clean dominant peak, so that the empirical relation (53) no longer applies. The FFT alone does not separate deterministic chaos from a dense quasi-periodic structure with many incommensurate frequencies, and we leave that question to the diagnostics identified in the limitations. When μ increases to 1, a finite set of well-defined peaks emerges and the relation (53) provides a good fit. At $\mu = 10$ (m_2 heavy), the spectrum of φ' sharpens into three narrow lines at $\nu \approx 0.60$, 1.20 and 1.79, which match the fundamental $\langle \varphi' \rangle / \pi$ and its first two harmonics: m_2 is too heavy to respond quickly, its motion is essentially periodic, and the spectrum approaches that of a near-linear oscillator. The shape of the spectrum thus changes qualitatively with μ, transitioning from a broadband response for small μ to a sparse harmonic structure for large μ, with the moderate-μ case showing an intermediate combinatorial pattern. This is the spectral counterpart of the progressive linearisation of m_2's response as its inertia grows.

Influence of the initial energy

Figure 10 compares the spectra for three energy levels, all with $\mu = 1$: a *low-energy* case ($\theta'_0 = 0.1$, $\varphi'_0 = 1.0$), the reference case, and a *high-energy* case ($\theta'_0 = 1.0$, $\varphi'_0 = 8.0$).

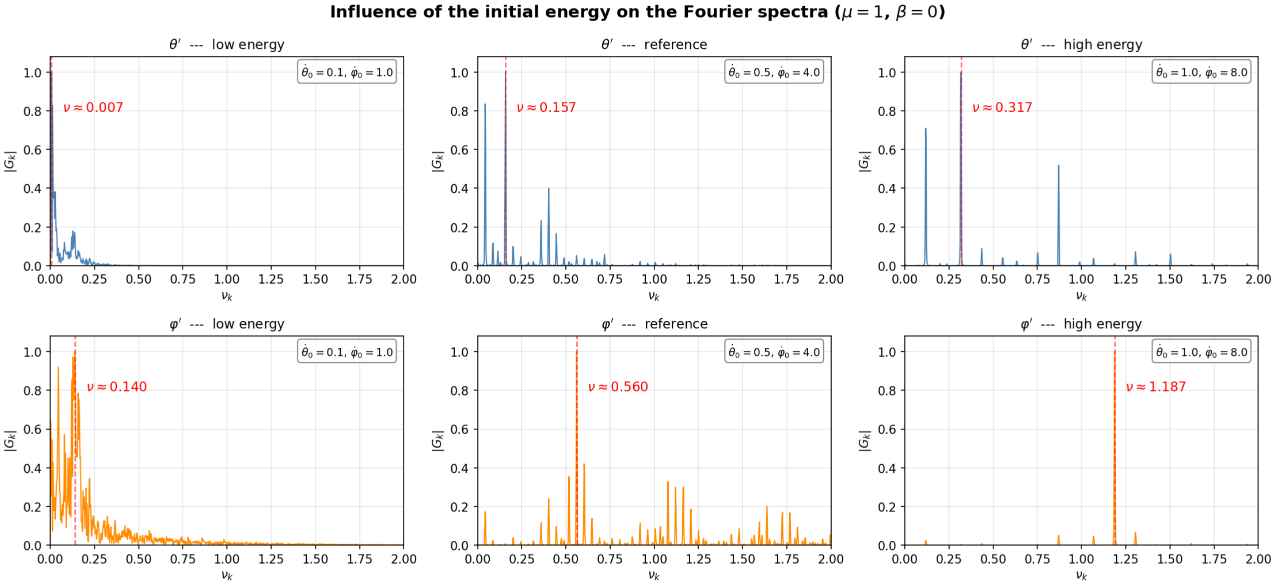

Figure 10: Influence of the initial energy on the Fourier spectra ($\mu = 1$, $\beta = 0$). Three sets of initial angular velocities are compared at fixed initial positions $\theta_0 = \pi/2$, $\varphi_0 = 0$.

At low energy, the motion remains close to the neighbourhood of the initial configuration and the spectrum concentrates at low frequencies with a dense, noisy structure: the trajectory explores a small region of phase space, and no clean dominant peak emerges. At reference energy, the spectrum broadens into a multi-peak structure, with both the fundamental and several combination frequencies clearly visible. At high energy, the masses rotate fast enough that the spring coupling acts essentially as a small perturbation on a dominant rotation. The spectrum of φ' collapses onto a single sharp peak at $\nu \approx 1.19$, which corresponds to $\langle\varphi'\rangle/\pi$ with $\langle\varphi'\rangle \approx 3.73$, in agreement with the empirical relation (53). This time-average is close to but smaller than $\varphi'_0 = 8$: even when the spring is weak, the geometric slowdown by $g(\varphi)$ persists and biases the time-average downward. The peak is therefore *not* located at the rotation frequency $\varphi'_0/(2\pi) = 1.27$, although the two values are numerically close.

Summary

The Fourier analysis confirms and quantifies what is visible in the phase portraits: in the moderate-μ and ordered-energy regimes investigated here, the conservative dynamics carries two characteristic frequencies whose sums and differences populate a comb of secondary peaks, the typical fingerprint of quasi-periodic motion on a two-frequency torus. In all the ordered cases tested, the dominant peak of each angular velocity is found at twice its time-averaged rotation frequency, $\nu \approx \langle\dot q\rangle/\pi$. This is reported as an empirical relation with a clear physical interpretation: the π-periodicity of $g(\varphi)$ in (54) accounts for the factor of two in φ', and the nonlinear combination of spring-force terms in (55) produces it for θ'. The relation has been verified across the regimes presented above; extending the test to a broader sweep of parameter space and deriving the precise amplitudes of the secondary peaks are natural extensions of this work. A clean spectrum of isolated peaks is observed in two limiting regimes: large μ (quasi-linear oscillator with well-defined harmonics) or high initial energy (dominant rotation with weak spring perturbation). At very low μ or very low energy, the spectrum becomes a broad continuum and the empirical relation no longer applies; classifying this regime as deterministic chaos, dense quasi-periodicity, or a long transient cannot be done from the FFT alone, and is identified as a target for future work.

8 Conclusion

This report has developed a complete analysis of a two-mass system in which m_1 slides without friction on a circle of radius R and m_2 slides on an ellipse of semi-axes $(3R/8,\ R/8)$ subject to viscous friction, the two masses being coupled by a linear spring of natural length $l_0 = R$. The study was built in three complementary layers: an analytical derivation of the model, a numerical exploration of its dissipative dynamics, and a frequency-domain interpretation of the conservative regime.

The first layer was analytical. The Lagrangian formalism yielded two coupled nonlinear equations of motion, while the generalised force formalism incorporated the viscous friction acting on m_2. The non-dimensionalisation reduced the problem to two governing parameters: the mass ratio $\mu = m_2/m_1$ and the dimensionless damping coefficient $\beta = \alpha/\sqrt{k\, m_1}$. The resulting energy balance, given in equation (44), shows that the rate of change of the total energy is reduced to a single non-positive term. This identifies the viscous force on m_2 as the unique dissipation channel of the system and explains why the conservative case is recovered exactly when $\beta = 0$.

The second layer was numerical. The dimensionless state-space system was integrated with an adaptive RK45 scheme at tight tolerances and validated against the analytical energy conservation law in the frictionless case, with a relative drift below 5×10^{-8}. In parallel, an interactive web-based simulator was developed and used as a full methodological component of the work: it provided real-time animation of the two constrained motions, dynamic plots of the energy decomposition and phase portraits, and live control of μ, β and the initial conditions. This tool supported the exploration of the parameter space, the selection of representative regimes, and the physical interpretation of the coupled dynamics before each systematic numerical sweep.

Two non-obvious results emerged from this numerical analysis. First, the dissipation is *non-monotonic* in β: moderate damping dissipates efficiently, whereas large damping immobilises m_2 in a quasi-static regime where the velocity becomes so small that the quadratic dissipation power nearly vanishes. As a result, the energy initially stored in the frictionless mass m_1 can only be extracted through a slow indirect pathway involving the spring coupling. Second, the final rest configuration of the dissipative system satisfies the exact geometric relation derived in equation (50). The numerical simulations verified this relation to machine precision, confirming that the system converges to a relaxed-spring configuration whose branch depends on the initial state.

The third layer was spectral. The conservative dynamics was analysed through the Fourier spectra of the angular velocities $\theta'(\tau)$ and $\varphi'(\tau)$, which remain bounded even though the angular positions themselves grow unboundedly. In the ordered regimes, the dominant peaks follow the empirical relation established in equation (53): each peak occurs at approximately twice the corresponding time-averaged rotation frequency. This factor of two has a clear physical origin. For φ', it follows from the π-periodicity of the geometric factor $g(\varphi)$, expressed in equation (54); for θ', it arises from the nonlinear spring-force structure and the frequency mixing made explicit in equation (55).

The spectra also reveal how strongly the dynamics depends on the mass ratio and the initial energy. Small μ or low energy produces a broadband response where the empirical frequency relation no longer applies, while large μ or high energy sharpens the spectrum into clean harmonic peaks and brings the system closer to a quasi-linear regime. The satellite peaks observed around the dominant frequencies are consistent with a coupled two-frequency motion, although a formal classification of the broadband regime would require additional tools such as Poincaré sections, Lyapunov exponents or frequency maps.

Taken together, the analytical, numerical and spectral results provide a coherent picture of the system dynamics and show how a geometrically constrained mechanical model can generate rich behaviour through the interaction of geometry, coupling and dissipation. Beyond the specific system studied here, the work illustrates the value of combining analytical derivation, numerical validation and interactive exploration to understand nonlinear dynamical systems.

9 Limitations and future work

Several simplifying assumptions of the present model open directions for future investigation.

Friction modelling. The viscous friction is modelled as a single linear term proportional to the velocity of m_2. More realistic tribological behaviour, such as Coulomb friction, Stribeck effects, or velocity-dependent coefficients, would modify the qualitative behaviour in the low-velocity regime and, in particular, would change the structure of the final rest state. Incorporating a non-linear friction law would also allow discussion of stick-slip phenomena that a purely viscous model cannot capture.

Mechanical idealisations. The spring is assumed to be linear and massless, and the masses are treated as point particles. Extending the analysis to a nonlinear spring (hardening or softening) would let the spring itself contribute to the frequency content, and accounting for a finite spring mass would introduce additional internal degrees of freedom. Similarly, the absence of gravity was inherited from the problem statement; reintroducing a gravitational field would create a proper equilibrium configuration, allow a classical linearisation around it, and enable a direct comparison of analytical eigenfrequencies with FFT peaks, an analysis that is not available in the present gravity-free setting.

Parameter-space exploration. The numerical exploration covered a representative but not exhaustive range of the parameter space. In particular, the mass ratio was restricted to $\mu \in [0.1, 20]$ and the damping coefficient to $\beta \in [0, 20]$, and the simulation horizon was limited to $\tau = 200$ for most figures (with a few excursions to $\tau = 5000$ to confirm asymptotic dissipation for heavy m_2). A more systematic sweep combined with a quantitative characterisation, for example Lyapunov exponents to assess the chaotic character suggested by the $\mu = 0.1$ spectra, or bifurcation diagrams as a function of the initial energy, would sharpen the informal observations made here. The interactive simulator could also be extended to display these quantitative indicators on the fly, turning it from an exploration tool into a measurement instrument.

Frequency analysis and stability. The frequency analysis focused exclusively on the conservative case.

Extending it to the lightly damped regime ($\beta \ll 1$) through a short-time or wavelet analysis would give access to the time evolution of the dominant frequencies as energy drains from the system, and would help quantify the rate at which each spectral peak decays. Finally, the exact equilibrium relation $\frac{3}{4}\cos\theta_{\mathrm{eq}}\cos\varphi_{\mathrm{eq}} + \frac{1}{4}\sin\theta_{\mathrm{eq}}\sin\varphi_{\mathrm{eq}} = (9\cos^2\varphi_{\mathrm{eq}}+\sin^2\varphi_{\mathrm{eq}})/64$ admits an infinite family of solutions, and a stability analysis identifying which branches are attractors as a function of the initial conditions would provide a useful companion to the dynamical results presented here.

References

Virtanen, P., Gommers, R., Oliphant, T. E., Haberland, M., Reddy, T., Cournapeau, D., Burovski, E., Peterson, P., Weckesser, W., Bright, J., van der Walt, S. J., Brett, M., Wilson, J., Millman, K. J., Mayorov, N., Nelson, A. R. J., Jones, E., Kern, R., Larson, E., … SciPy 1.0 Contributors. (2020). *SciPy 1.0: Fundamental algorithms for scientific computing in Python. Nature Methods, 17*, 261–272. https://doi.org/10.1038/s41592-019-0686-2